1   **NUMERICAL PREDICTION OF UNDRAINED RESPONSE OF PLATE**

2   **ANCHORS UNDER COMBINED TRANSLATION AND TORSION**

3   **Hamidreza Nouri[1], Giovanna Biscontin[2] and Charles P. Aubeny, M. ASCE[3]**

4

5   **ABSTRACT**

6   The undrained pure translational and torsional capacity of anchors and the plate response un-

7   der eccentric translational loading is investigated in this paper using three-dimensional finite

8   element (3D-FE) analysis. Plastic limit analysis is adopted to establish a benchmark solution

9   for ultimate translational resistance with satisfactory agreement with the FE values which

10   confirms the developed numerical model. Although plate thickness has a marked impact on

11   the maximum shear and torsion resistance, the shape of failure envelope is minimally affected

12   by thickness. A simple three-degree-of-freedom interaction equation is curve-fitted to FE

13   failure datapoints. Representative interaction relationships are introduced for square and rec-

14   tangular plates.

15

16   KEY WORDS: plate anchor; torsional capacity; translational (shear) resistance; plastic limit

17   analysis; finite element analysis; failure envelope.

[1] Project Geotechnical Engineer, Golder Associates, Inc., 18300 NE Union Hill Road, Suite 200, Redmond, Washington, USA 98052, E-mail: Nouri.hreza@gmail.com

[2] University Lecturer in Geotechnical Engineering, Department of Engineering, University of Cambridge, Schofield Centre, High Cross, Madingley Road, Cambridge CB3 0EL, UK, E-Mail: gb479@eng.cam.ac.uk

[3] Professor, Texas A&M University, 3136 TAMU, College Station, TX 77843-3136, USA (corresponding author). E-mail:caubeny@civil.tamu.edu

1- Introduction

The offshore industry is expanding farther into very deep water, leading to a number of economical and technical challenges. Floating structures anchored to the seabed using catenary and taut-wire mooring systems are generally more technically feasible and cost effective than gravity based platforms in these deep water environments. Anchorage for floating systems can include piles, caissons and various types of plate anchors. This paper addresses performance of the latter alternative. Under normal operating conditions, plate anchors are mainly subjected to pull-out loading in an intended plane of loading, for example, the X-Z plane in Fig. 1(a). However, extreme storm events may cause partial failure with the loss of one or several mooring lines resulting in substantial changes in the orientation of the intact lines, as well as to the applied resultant force [Fig. 1(b)]. Under these conditions the anchor must resist a general system of loads, with some components of load acting outside the plane of intended loading.

A full description of behavior of an anchor plate in a partially failed mooring system requires adequate understanding of undrained response of anchor plates subjected to general loading conditions involving six degrees of freedom. This entails characterizing anchor behavior for six components of uniaxial loading (3 translational and 3 rotational) as well as the interaction effects amongst all possible load combinations. Much of the research in this area to date has focused on in-plane loading conditions involving forces in the X and Z directions and moments about the Y-axis (Fig. 1) (O'Neill et al. 2003, Murff et al. 2005). This paper investigates anchor behavior for loading in the X-Y plane in Fig. 1, which will be termed 'shear-torsional' loading. The loading comprises 'shear' forces H_x and H_y and a torsion T; i.e., a moment acting about the Z-axis. All loads act within the plane of the plate. The study presented herein does not attempt to fully characterize anchor behavior for general 6 degree of freedom loading conditions. Rather, it investigates a critical component for a more general model to be developed in the future.

42   The plate anchors considered in this paper are idealized as rectangular plates with specified aspect

43   ratios (*W/L*) and thickness t (Fig. 1). Some plate anchors, such as suction embedded plate anchors

44   (SEPLAs) match this idealized geometry to a reasonable degree. By contrast, drag embedded plate

45   anchors usually have relatively complex geometric configurations to facilitate embedment. The

46   findings of this paper can provide useful insights into the behavior of drag anchors, but the inher-

47   ent limitations of the analyses arising from the simplified geometry must be carefully considered.

48   O'Neill et al. (2003) used plane strain finite element (2D-FE) analysis to investigate the behavior

49   of rectangular and wedge-shaped strip anchors subjected to combined in-plane translational, verti-

50   cal, and rotational loading. They also developed plastic upper bound solutions to evaluate pure

51   parallel, normal, and rotational capacity factors for strip plates to validate the FE results. Using

52   two-dimensional finite element (2D-FE) analysis, they produced failure loci and plastic potentials

53   from considerations of fluke-soil interaction and then developed a design method to predict drag

54   anchor trajectory during embedment. Murff et al. (2005) used 2D-FE to develop a failure locus for

55   the ratio of plate length to thickness (*L/t*) of 7 and 20 with different plate roughness. Yang et al.

56   (2010) employed 3D-FE, to study the behavior of infinitely thin plate anchors subjected to loading

57   in all six degrees of freedom. They also introduced a plasticity solution for failure envelope of a

58   plate under combined translation-torsion and developed formulas to estimate pure sliding and tor-

59   sional bearing capacity. This plasticity solution predicts the behavior of an infinitely thin plate, but

60   provided only an approximate solution for a plate with finite thickness. Nouri (2013) modified the

61   plastic limit solution originally developed by Yang et al. (2010) to predict more accurately the tor-

62   sional collapse load and failure envelopes of a plate anchor with finite thickness. Researchers have

63   also conducted 3D-FE analysis on other types of offshore foundations under general loading con-

64   dition, such as for mudmats (Feng et al. 2014) or OMNI-max anchor (Wei et al. 2015).

65   In the current study, we use 3D-FE analysis to evaluate the translational (parallel to plate) and tor-

66   sional ultimate bearing capacity of plates, as well as the interaction of these two modes of loading.

67 Results of the FE analysis are also used to validate analytical solutions to predict bearing capacities and to confirm whether the postulated failure mechanism for the analytical solution is correct.

68 ties and to confirm whether the postulated failure mechanism for the analytical solution is correct.

69 **2- Material Properties for Numerical Model**

70 The commercial software *ABAQUS* (HKS, 2008) is used in this study. The plate is assumed to be

71 deeply embedded, with localized plastic flow forming around the plate anchor and not extending

72 to the surface, resulting in capacity factors that are not affected by overburden and soil weight

73 (Song et al. 2008; Wang et al. 2010). Thus, the soil is assumed to be a weightless material without

74 loss of accuracy. Since the size of the plastic zone around the plate anchor at failure is smaller for

75 shear and torsion than for uplift and rotation, the assumption of deep embedment is valid even for

76 shallower embedment depths. This assumption also implies that the soil and plate are fully bond-

77 ed. Thus, "no separation" is assumed as the normal (i.e. perpendicular to interface) contact behav-

78 ior for the plate-soil interface in conjunction with "rough" for the tangential contact property to

79 realistically simulate a fully bonded condition. The interaction between soil and plate is modeled

80 using surface to surface contact pairs in which the plate outer surface is chosen as a "master sur-

81 face" and the soil surface in contact with the plate as a "slave surface". The active degrees of free-

82 dom of the nodes on the slave surface are constrained to the master surface nodes through rela-

83 tionships which define the tangential and normal interaction at the nodes of these two surfaces.

84 Clay under undrained conditions is modeled as a linear elastic perfectly plastic material, with

85 yielding determined by the Von Mises failure criterion with undrained shear strength, s_u. The

86 Young's modulus of the soil, E, is given by a modulus ratio of $E/s_u = 500$, and Poisson's ratio is

87 taken as 0.49 to simulate no volume change for undrained clay in total stress analysis. The ulti-

88 mate capacity of the plate is not affected by the pre-failure elastic behavior of the soil (Chen and

89 Liu 1990). In addition, in studies on plate uplift bearing capacity it was observed that as the soil

90 rigidity (E/s_u) increases, the anchor displacement required to mobilize the maximum capacity re-

91 duces, while the maximum capacity does not change (Song et al. 2008; Wang et al. 2010). There-

92   fore, the Young's modulus of the soil is assumed constant in these studies. Since the analysis of

93   the structural behavior of the anchor is not within the scope of this work, the plate is modeled as a

94   rigid body with Young's modulus 10^{10} times that of the soil, and Poisson's ratio of 0.30. The

95   analysis is conducted using small strain displacement control, since the ultimate translational and

96   torsional capacities are developed within an anchor movement of 0.1 times the anchor length. A

97   reference node is defined in the center of the plate and prescribed displacements are applied at the

98   reference point to perform displacement controlled analysis. Standard boundary conditions are al-

99   so applied to the model: the base is fixed in all directions, while the vertical boundaries are fixed

100 in the lateral direction and free to move vertically. In all the models with a plane of symmetry, the

101 nodes on the plane of symmetry are only allowed to move in the plane.

102 **3- Challenges of the Numerical Modeling**

103 Unrealistic stress distributions arise from the displacement discontinuities that take place at the

104 edges of a rigid structure penetrating a softer material (Van Langen and Vermeer 1991) resulting

105 in higher overall resistance. The unfavorable effect on the numerical results is more severe for

106 buried structures and materials with no volume change. There are mainly two approaches to over-

107 come such loss of numerical accuracy:

108   1- Mesh refinement

109   2- Contact pairs along the corners of the plate

110 As plane strain 2D analyses take much less time and fewer memory resources, they are a reliable

111 and fast way to evaluate possible solutions for this problem. 2D-FE analyses can also be adopted

112 to develop an optimal mesh size and to verify properties and length of the contact pairs in soil

113 along the plate corners through sensitivity analysis. The plate anchor is idealized as a strip with

114 length L and thickness t in 2D space.

115   **3-1- Mesh refinement around the sharp edges**

116   As the detrimental effect of the stress concentration is more pronounced in thinner plates, a plate

117   with thickness of $t = L/20$, is considered for the preliminary 2D analysis to calculate the ultimate

118   translational (parallel to plate) bearing capacity of the strip plate. Several 2D models with coarse,

119   fine, and very fine mesh with first order 4-node plane strain quadrilateral hybrid elements,

120   CPE4H, are created. All the soil elements are fully integrated hybrid type to accommodate the

121   constant volume constraint in undrained conditions. The whole model dimensions are $9L \times 9L$, in

122   which L is the length of the plate. The model is divided into several zones with different mesh

123   densities to minimize the degrees of freedom of the model and avoid unnecessary computational

124   effort. The finest zone extending to $t = L/20$ around the plate consists of square elements with di-

125   mension of $L/80$, $L/160$, $L/320$ for the coarse, fine, and very fine meshes, respectively. A fine

126   mesh with second order hybrid square elements (CPE8H) with dimension of $L/160 \times L/160$ is also

127   created to assess the performance of higher order elements in predicting ultimate bearing capacity.

128   Only a small difference can be observed in the maximum parallel bearing capacity of the plate for

129   the fine and very fine meshes in Fig. 2. The results from the fine mesh (elements of $L/160 \times L/160$)

130   with second order elements match exactly the values of parallel bearing capacity from the very fi-

131   ne mesh with first order elements. Refining the mesh improves the results and overcomes the is-

132   sues of stress concentration to some extent, but the bearing capacity values do not change signifi-

133   cantly after some degree of mesh refinement. The ultimate shear capacities calculated using the

134   very fine mesh or higher order elements are still 13% higher than the value obtained from the up-

135   per bound plastic limit analysis. In addition, a 3D fine mesh with elements of size $L/160 \times L/160$

136   would require significant computational effort, making the numerical analysis practically impossi-

137   ble to conduct. Thus, for a reasonable computational effort it seems that excessive mesh refine-

138   ment fails to provide sufficiently accurate FE results for shear bearing capacity of plate anchors

139   deeply embedded in undrained clay.

140   **3-2- Contact interfaces in soil along the corners of the plate**

141   An alternative solution to enhance the stress distribution on the plate edges is using contact inter-

142   faces near the corners of the plate. Rowe and Davis (1977) introduced potential rupture lines near

143   the edge of an anchor to ensure accurate modeling of the singularity at the anchor tip. This ap-

144   proach attempted to overcome the inhibition of free plastic flow inherent in the usual stiffness

145   formulation of the FE method by permitting the formation of velocity discontinuities in the re-

146   gions of high stress and velocity gradient near the tip of the anchor plate (Rowe and Davis, 1977).

147   Van Langen and Vermeer (1991) introduced zero-thickness interface elements to enhance the un-

148   realistic stress non-uniformity on surfaces with singular points.

149   Using the same general concept, and taking advantage of *ABAQUS* capabilities in defining various

150   types of contact relationships, this study adopts interfaces placed vertically and horizontally in the

151   soil in the vicinity of plate corners to accommodate for vertical and horizontal displacement dis-

152   continuities. Each interface is defined as a couple of master and slave surfaces in the soil that can

153   slide independently from each other according to a surface to surface contact relationship (contact

154   pairs). A coefficient of friction ($\mu = 0.001$) and a maximum contact shear stress equal to the un-

155   drained shear strength of the soil ($\tau_{max} = s_u$) are adopted to simulate frictional behavior. No separa-

156   tion between the master and slave surface nodes is also assumed in the direction normal to the in-

157   terface.

158   As shown by O'Neill et al. (2003) and confirmed through the 2D-FE analysis, in-plane horizontal

159   movement of the rigid plate creates a plastic zone in the soil around the plate that extends for a

160   distance from the plate approximately equal to plate thickness, t. Contours of deformation in the x

161   direction for a plate under pure sliding in the 2D-FE analysis shown in Fig. 3 also confirm the ex-

162   tents of this plastic zone. The 3D-FE analysis also shows a similar zone of thickness t to be affect-

163   ed by the torsional rotation (Fig. 4). The finest zone wrapping around the plate contributes the

164   most to the number of elements, i.e. the computational effort in the model.

165   Thus, this region extends for a distance from the plate equal to the plate thickness, t, to minimize

166   the number of elements. The length of the contact is also adopted equal to plate thickness. The fi-

167   nal 2D mesh and the contacts placed horizontally and vertically in the vicinity of the plate corners

168   are shown in Fig. 5. The final mesh is divided into six different zones with element size decreas-

169   ing as the zones become closer to the plate. Mesh tie constraints are used to constrain each active

170   degree of freedom of the slave node on the finer zone surface to the master node on the coarser

171   zone surface. FE results for the ultimate parallel bearing capacity are compared with the plastic

172   limit analysis (PLA) value presented by O'Neill et al. (2003). For a plate with $t = L/20$ and

173      $\mu=0.001$, the FE-derived value of the plane strain shear bearing capacity factor is 2.77, which ex-

174   ceeds the PLA result, 2.75, by less than 1%. The effect of the interface coefficient of friction, μ,

175   on the ultimate shear capacity results is evaluated for coefficient values ranging from 0.001 to

176   1000 (Fig. 6). For higher values of friction coefficient the ultimate capacity increase to about 2.85

177   and remains constant for coefficient values larger than one ($\mu > 1$), which shows a minor impact of

178   the friction coefficient on the results. Thus, the friction coefficient of $\mu=0.001$ is adopted for the

179   interface in all the following analysis. FE results for the ultimate parallel bearing capacity also in-

180   dicate that the mesh is adequately fine, contact length and properties are reasonable and the equiv-

181   alent 3D mesh could give satisfactory results.

182   **4- 3D finite element analysis**

183   The 3D mesh is created with the same approach used for the 2D mesh (Fig. 7). The 3D model is

184   created for anchors idealized as square and rectangular ($W/L = 2.0$) plates with thickness $t = L/20$,

185      $L/14$, $L/10$, and $L/7$. The model dimensions are $9L \times 9L \times 5L$ and $9L \times 12L \times 5L$ for the square and rec-

186   tangular plates, respectively. The 3D mesh consists of 8-node full integration 3D hybrid first order

187   elements, C3D8H. Similarly to the 2D analyses, the Von Mises constitutive model with the same

188   elastic-plastic properties is used for the soil. The contact definition of the 2D model is used at the

189   plate corners in the soil and plate-soil interface. The length of the contact and the depth of the fine

190   mesh zone around the plate are equal to the plate thickness in all models (Fig. 4). Taking ad-

191   vantage of the symmetric nature of shear-torsion loading of the plate anchor, only half of the FE

192   mesh is simulated. Standard boundary conditions are applied to the model boundaries and plane of

193   symmetry.

194   **4-1- Ultimate load capacity**

195   In-plane translational (parallel to plate) displacements are applied in the direction parallel to the

196   smaller (L) and larger (W) sides of the plate (x and y directions respectively) and torsion is pre-

197   scribed as the rotation of the plate about the z axis. The FE results for the pure shear and pure tor-

198   sional loading are reported in Tables 1 and 2, respectively, for square and rectangular ($W/L = 2$)

199   plates, in their normalized forms, $N_{sx,max}$, $N_{sy,max}$, and $N_{t,max}$, where:

$$N_{sx,\max} = \frac{H_{x,\max}}{LWs_u} \tag{1}$$

$$N_{sy,\max} = \frac{H_{y,\max}}{LWs_u} \tag{2}$$

$$N_{t,\max} = \frac{T_{\max}}{L^2 Ws_u} \tag{3}$$

200   where H_x, and H_y, are the horizontal (shear) reaction force in x and y directions and T is the tor-

201   sional reaction moment of the rigid anchor plate about the z axis.

202   The FE ultimate shear resistance is compared with benchmark solutions: (1) the resistance factor

203   for an infinitely thin plate, which provides the minimum values of ultimate shear resistance

204   ($N_{sx,max}=N_{sy,max}=2$ for $H_{x,max}=H_{y,max}=2s_uWL$); (2) A PLA formulation, developed by Yang et al.

205   (2010) to evaluate the plate thickness impact on the ultimate shear capacity (Table 1):

206    $$N_{sx,max} = \frac{H_{x\max}}{s_u LW} = 2\alpha + 2\left[\alpha \frac{L}{W} + N_e\right]\frac{t}{L} \tag{1}$$

207    $$N_{sy,max} = \frac{H_{y\max}}{s_u LW} = 2\alpha + 2\left[\alpha + N_e \frac{L}{W}\right]\frac{t}{L} \tag{2}$$

208   where N_e is the simple plane strain bearing capacity factor, equal to 7.5 (O'Neill et al. 2003). The

209   adhesion factor, α, for the fully bonded condition is assumed equal to unity. The above expression

210   for pure x-shear capacity factor, $N_{sx,max}$, for a strip plate ($L/W \approx 0$) reduces to $N_{s,max}=2(1+N_e.t/L)$ as

211   proposed by O'Neill et al. (2003) for ultimate parallel plate capacity in 2D plane strain condition.

212   Whereas the PLA analyses under-predict FE shear capacity factors for plate thickness of $t = L/20$,

213   and $L/14$, they over-predict FE capacity factors for $t = L/10$ and $L/7$ for both square and rectangu-

214   lar plates. This could be attributed to the fact that the shear bearing capacity of thicker plates is

215   less sensitive to stress concentration on plate corners because the ultimate shear bearing capacity

216   of thick plates is larger than that of thinner ones. Overall, the 1-3% difference between PLA and

217   FE results for ultimate shear capacity is minimal. The thickness has a marked impact on the plate

218   shear resistance, resulting in an approximately 40 to 120% increase for square plates of $t=L/20$ and

219   $L/7$ respectively, compared to the $t=0$ plate. The typical normalized load-displacement responses

220   for square and regular plates under in-plane y-shear are also depicted in Fig. 8.

221   Table 2 summarizes the FE derived maximum torsional resistance. Torsion-rotation plots are also

222   included in Fig. 9. Yang et al. (2010) also proposed a PLA solution for pure torsion, which tends

223   to over-predict resistance for plates of finite thickness (Nouri 2013), but their formulation for an

224   infinitely thin plate ($N_{t,max0}$) provides a lower bound value for ultimate torsional resistance:

$$N_{t,\max 0} = T_{max0} / (s_u WL^2) =$$

225   $$\alpha \frac{(W/L)^2}{6}\left\{\frac{\sin\theta_o}{\cos^2\theta_o} + ln\left[\tan\left(\frac{\pi}{4}+\frac{\theta_o}{2}\right)\right]\right\} + \alpha \frac{L/W}{6}\left\{\frac{\cos\theta_o}{\sin^2\theta_o} - ln\left[\tan\left(\frac{\theta_o}{2}\right)\right]\right\} \qquad (3)$$

226   where $\theta_o = \tan^{-1}(L/W)$. For square and rectangular plates this analytical solution yields 0.76 and

227   1.19, respectively. Torsional resistance also increases markedly with plate thickness by approxi-

228   mately 40 to 90% for $t=L/20$ and $L/7$, respectively, versus the zero thickness plate.

229   **4-2- Failure envelopes**

230 In order to construct the interaction curve or failure locus, two types of displacement control

231 methods are used: the swipe test and the probe test. In the swipe test approach failure locus is ob-

232 tained by a single analysis in two separate steps. In the swipe test the plate is firstly displaced in

233 the direction of the degree of freedom (DoF) under examination from zero until the ultimate ca-

234 pacity in that direction is reached. In the second step, the displacement is imposed in the second

235 DoF until the ultimate capacity in the new direction is fully developed. In the finite element analy-

236 sis once the ultimate force is reached in the first step, there will be no more increase in the reac-

237 tion force along that DoF, thus no further expansion in overall plate failure locus as the movement

238 of the plate progresses. The disadvantage of this method is that, due to the elasto-plastic "yield-

239 ing" occurring within the "failure" locus, the swipe test tracks a load path marginally inside the

240 actual overall plate failure envelope (Bransby and Randolph 1998).

241 In the probe test or fixed displacement method, a single point on the failure envelope is identified

242 for each fixed ratio of the prescribed displacements. Therefore, the failure locus can be created by

243 conducting a number of finite element analyses with different displacement ratios. The prescribed

244 fixed displacement ratio gives rise to a load path beginning at the origin with an initial gradient

245 based on the elastic stiffness of the material. The path gradient decreases as approaching failure

246 envelope to follow the interaction curve and stops where there is no further increase in the forces

247 developed in each intended degree of freedom (Bransby and Randolph 1998). This method gives

248 an accurate trace of the failure envelope, but requires several FE analyses.

249   *4-2-1- Combined in-plane shear and torsion*

250 Fig. 10 shows examples of the swipe and probe failure envelopes for square and rectangular plates

251 of $t= L/7$ subjected to in-plane y-translation and torsion ($N_{sy} - N_t$). The rest of the analyzed cases

252 are not included for brevity. Note that $du_y/d\phi$ is the prescribed fixed displacement ratio for each

253 probe path, defined as the ratio of plate displacement increment in the y direction, to the increment

254 of the plate in-plane rotation. The probe curve exceeds the shear-torsion (i.e. shear prescribed first,

255 torsion next) swipe envelope. This difference increases significantly if a torsion-shear swipe test

256 (i.e. torsion first, shear next) is carried out instead. In the torsion-shear swipe test, at the moment

257 of full development of the torsional ultimate capacity, the soil elements in regions close to the

258 middle of the plate and the plate sides are not completely plastic yet since the maximum dis-

259 placements occur in the region next to the corners of the plate (See Fig. 4). Thus, the stress state of

260 the soil elements in the center is farther from failure at the end of the first stage of pure torsion. In

261 contrast, in the shear-torsion swipe test, all the soil surrounding the plate is fully plastic at the end

262 of full mobilization of the shear resistance. All the swipe tests follow the shear-torsion sequence.

263 As Fig. 10 suggests and as it was discussed earlier in the paper, the probe test approach offers

264 more accurate values since the swipe envelope travels although marginally but still inside the

265 probe curve. Therefore, probe test values are adopted and referred as FE results hereafter in the

266 paper.

267 The failure envelope (e.g. Fig. 10) can be described by two basic components:

268 1- Maximum plate resistance under pure shear ($H_{x,max}$, $H_{y,max}$) and torsion (T_{max}) which quanti-

269   fies the size of the envelope (discussed in previous section).

270 2- The shape of the failure envelope defined by the shear or torsional resistance normalized

271   by the corresponding maximum value (e.g. $N_{sy}/N_{sy,max}$ -$N_t/N_{t,max}$ or $H_y/H_{y,max}$ - T/T_{max}).

272 Fig. 11 summarizes the FE probe results in the normalized space for all the studied cases. Interest-

273 ingly, the plate thickness does not seem to affect the interaction behavior of the plate under one-

274 way planar shear and torsion for the range of analyzed plate thicknesses, which is typical in prac-

275 tice. The interaction response is instead affected by plate aspect ratio and the direction of transla-

276 tion. Thus, a best fit for each aspect ratio and eccentric translation can be adopted as a representa-

277 tive failure envelope (Fig. 11).

278 The FE derived envelopes are compared with a PLA analytical solution, which was originally de-

279 veloped by Nouri et al. (2014) for surface foundations (i.e. zero embedment) under combined in-

280 plane translation and torsion. The formulation is slightly modified for a deeply embedded plate of

281 zero thickness under the same loading combination. Adopting a PLA solution for zero plate thick-

282 ness ($PLA_{t=0}$) has several advantages:

   - It makes the PLA formulation easier and more manageable for excel spreadsheet applications

      and provides a straightforward benchmark solution for FE failure envelopes.

285   - Insensitivity of the normalized interaction response to plate thickness (Fig 11), makes the

286      $PLA_{t=0}$ a simple yet reliable benchmark solution to evaluate the shape of failure envelope in

287   normalized space for other plate thicknesses. Details of the proposed PLA formulation are

288   summarized in Appendix A.

289 Fig. 12 compares the $PLA_{t=0}$ failure envelopes with FE values. Overall, the $PLA_{t=0}$ compares very

290 well with the FE failure points for the square plate, slightly overestimates the resistance of rectan-

291 gular plates under eccentric shear in x-direction, and underpredicts the bearing capacity for rectan-

292 gular plates subjected to shear y-torsion. Besides providing a beneficial benchmark, $PLA_{t=0}$ poten-

293 tially offers a simplified, yet effective, approach for finite thickness plates, if combined with the

294 ultimate resistance factors for shear ($N_{sx,max}$ and $N_{sy,max}$) for $t{\neq}0$ (Nouri et al. 2014).

295 ***Shear capacity reduction with eccentricity***

296 Plotting the plate shear resistance versus the eccentricity offers an alternative and more intuitive

297 portrayal of the plate shear capacity reduction with associated torsion. Fig. 13(a) shows examples

298 of FE shear capacity reduction plots versus eccentricity for rectangular and square plates of $t=L/7$.

299 The y-sliding capacity reduction plots for square and rectangular plates are equivalent to shear y-

300 torsion failure envelopes in Fig. 10. Since the shear capacity in Fig. 13(a) is expressed as

301 $N_s=H/WLs_u$, the plots include both the size and shape elements for constructing a failure envelope.

302 Similarly to Fig. 11, Fig. 13(b) summarizes all the FE results with a best fit load reduction curves,

303 but in (H/H_{max} - e/L) space. Fig. 13(b) indicates that plates of higher aspect ratio are more effec-

304 tive in resisting eccentric loads than square plates, irrespective of the orientation of the plate with

305   respect to shear. However, eccentric sliding in x-direction perpendicular to the longer side of the

306   plate tends to reduce the shear capacity more significantly than eccentric y-sliding. The same trend

307   was also observed in PLA capacity reduction curves for surface foundations (Nouri et al. 2014).

308   *4-2-2- Co-planar shear (combined shearx-sheary)*

309   FE analyses are also conducted to determine the interaction response of square and rectangular

310   (W/L=2) plates of $t= L/20$ and $L/7$ under combined co-planar shear. Typical FE examples of swipe

311   and probe envelopes for N_{sx}-N_{sy} are summarized in Fig. 14 for rectangular plate of $t = L/7$.

312   The shape of the co-planar normalized failure envelope in the $H_x/H_{x,max}$-$H_y/H_{y,max}$ space (Fig. 15)

313   is approximately the same for all plate thicknesses and aspect ratios. Therefore, a single curve for

314   the FE data could be used to describe the normalized interaction response of plates with various

315   thicknesses and geometries. The normalized co-planar shear ($H_x/H_{x,max}$-$H_y/H_{y,max}$) failure envelope

316   can be described using the following equation:

$$f\left(H_x, H_y\right) \; = \; \left(\frac{H_x}{H_{x,max}}\right)^{hx} + \left(\frac{H_y}{H_{y,max}}\right)^{hy} - 1 = 0 \qquad (4)$$

317   Curve fitting yields interaction factors of hx=hy=2.5. For a zero thickness plate moving along any

318   arbitrary in-plane direction, the plate shear resistance factor is always constant and equal to 2 re-

319   gardless of the direction of plate translation. A constant resistance factor results in a circular locus

320   with radius of 2 in the N_{sx}-N_{sy} space and a circle of radius 1 in $H_x/H_{x,max}$-$H_y/H_{y,max}$ space (i.e.

321   hx=hy=2.0 as shown in Fig. 15). This concept has also been validated through PLA by Nouri

322   (2013). Comparison of circular (t=0) and FE shear$x$-shear$y$ envelopes in Fig. 15 suggests that even

323   a slight increase in plate thickness increases the plate shear resistance against the reduction in-

324   duced by another shear force applied in the perpendicular direction. This increase tends to be in-

325   sensitive to plate thickness at least for $t \leq L/7$ or changes in plate aspect ratio.

326   **4-3- Interaction equation**

327   Eq. (4) for concentric in-plane shear forces can be generalized for eccentric planar loads:

$$f(H_x, H_y, T) = \left[\left(\frac{H_x}{H_{x,\max}}\right)^{hx} + \left(\frac{H_y}{H_{y,\max}}\right)^{hy}\right]^h + \left(\frac{T}{T_{\max}}\right)^{mz} - 1 = 0 \qquad (5)$$

328    $f(H_x, H_y, T) = 0$ represents an ellipsoid in the $H_x/H_{x,\max}$ - $H_y/H_{y,\max}$ - T/T_{max} normalized space.

329   Since failure envelopes in the normalized space seem to be insensitive to plate thickness, the in-

330   teraction factors of hx, hy, h, and mz are determined by curve fitting Eq. (5) to all FE best fit fail-

331   ure envelopes for the square and rectangular plates in Figs. 11 and 15. Table 3 summarizes the

332   calculated interaction factors.

333   **5- CONCLUSIONS**

334   The purpose of this study is to evaluate pure translational and torsional ultimate plate capacity, as

335   well as to study the behavior of deeply embedded square and rectangular plates of finite thickness

336   under combined co-planar shear and torsion using 2D and 3D finite element (FE) simulations.

337   This study indicates the following:

338   1. Very fine meshes and higher order elements do not sufficiently eliminate stress concentration

339   and overprediction of capacity for a deeply embedded plate in undrained condition. Applica-

340   tion of contacts in the vicinity of the plate corners in soil improves bearing capacity esti-

341   mates. The ultimate sliding and torsional capacities, as well as the interaction factors, are re-

342   ported for a range of plate thicknesses and aspect ratios common in practice (Tables 1-2 and

343   Figs. 8-9).

344   2. Plate shear resistance begins to reduce even at small eccentricity (e.g. 5% reduction for

345   e/L=0.1 for square plate as shown in Fig. 13). Shear capacity reduces at a higher rate for

346   larger eccentricity (e.g. 50% shear capacity reduction for e=0.5L or eccentric shear force at

347   the edge of square plate).

348   3. Reduction in shear resistance is affected slightly by the plate thickness but essentially de-

349   creases with plate aspect ratio, since square plates are more vulnerable to reduction of sliding

350   capacity compared to rectangular plates (Fig. 13). In general, an eccentric shear load parallel

351   to the shorter side of the plate induces greater capacity reduction in rectangular plates.

352   4. Thickness has a marked effect on a plate shear and torsional resistance. For perspective, the

353   shear resistance factor equal to $N_s=2$ for a zero thickness plate, increases to about 4.4 for a

354   square plate with $t=L/7$ (more than 100% increase). Similarly, the torsional resistance factor

355   (N_t) increases by about 90% for square and rectangular plates with $t=L/7$.

356   5. The shape of the shear-torsion failure envelope in the normalized space (H/H_{max} - T/T_{max}) is

357   insensitive to plate thickness (Fig. 11). This facilitates the application of analytical solutions

358   developed for infinitely thin plates, PLA$_{t=0}$, (Nouri et al. 2014) to estimate the shape of the

359   failure envelope, which shows a reasonable agreement with FE values (Fig. 13). As shown in

360   Fig. 11, the shape of the shear-torsion failure envelope is affected by aspect ratio and the di-

361   rection of the eccentric shear force.

362   6. The shape of the co-planar shear (shear$x$-shear$y$) failure envelope is generally insensitive to

363   plate geometry and thickness, at least for the cases examined (Fig. 15).

364   7. A simple relationship is proposed to describe the failure envelope in the normalized space

365   ($H_x/H_{x,max}$ - $H_y/H_{y,max}$ - T/T_{max}). Taking advantage of the insensitivity of the shape of the fail-

366   ure envelope to thickness, a representative envelope and the associated interaction factors are

367   sufficient for practical design applications.

368

369 **APPENDIX A. PLA virtual work formulation for zero thickness plate**

370 For a horizontal load H applied at a distance e from the center of the plate (Fig A.1), equating ex-

371 ternal virtual work $\dot{W}$ to internal energy dissipation yields to:

372 $\quad H = \dot{D}/(\rho + e)\dot{\beta}$ $\hfill$ (A.1)

373 where $\dot{\beta}$ is a virtual angular velocity of the plate about a rotation center located a distance ρ from

374 the center. The rate of internal energy dissipation $\dot{D}$ is calculated by integrating the soil resistance

375 times the local velocity over the plate area:

376 $\quad \dot{D} = 2s_u\, \dot{\beta} \int_{-W/2}^{W/2} \int_{-L/2}^{L/2} \sqrt{(\rho + x)^2 + y^2}\, dxdy$ $\hfill$ (A.2)

377 The dissipation term ($\dot{D}$) in the proposed solution is two times the $\dot{D}$ for a surface foundation

378 (Nouri et al. 2014), since the energy is dissipated along both top and bottom faces of the plate.

379 This factor of 2 in the dissipation term is the only difference between this derivation and the PLA

380 formulation for surface foundations (Nouri et al. 2014).

381 A least upper bound collapse load is obtained by minimizing H with respect to ρ, which leads to:

382 $\quad H = \dfrac{1}{\dot{\beta}} \dfrac{\partial \dot{D}}{\partial \rho}$ $\hfill$ (A.3)

383 The collapse load (H) for the case of zero plate thickness becomes:

384 $\quad H = 2s_u \int_{-W/2}^{W/2} \int_{-L/2}^{L/2} \dfrac{\rho_{opt} + x}{\sqrt{(\rho_{opt} + x)^2 + y^2}}\, dxdy$ $\hfill$ (A.4)

385 where ρ_{opt} is the distance to the optimal center of rotation corresponding to a least upper bound.

386 Evaluation of the integral yields the following closed-form expression for H:

$$H = 2s_u \left[a_1^2 \ln \left| \frac{b_1 + W/2}{b_1 - W/2} \right| - a_2^2 \ln \left| \frac{b_2 + W/2}{b_2 - W/2} \right| + W(b_1 - b_2) \right]$$

$$a_1 = \rho_{opt} + L/2$$

387 $\quad a_2 = \rho_{opt} - L/2 \qquad\qquad\qquad\qquad\qquad\qquad\qquad\qquad\qquad\qquad\qquad$ (A.5)

$$b_1 = \sqrt{a_1^2 + W^2/4}$$

$$b_2 = \sqrt{a_2^2 + W^2/4}$$

388   The eccentricity, e, associated with any arbitrarily selected ρ is calculated from Eq. (A.1) with $\dot{D}$

389   and H evaluated and substituted from Eqs. (A.2) and (A.4), respectively. Analytical integration of

390   Eq. (A.2) is unwieldy; however, reduction to single integration is possible to facilitate simple de-

391   sign spreadsheet calculations:

$$\dot{D} = 2s_u \dot{\beta} \int_{-W/2}^{W/2} \left[(a_1 c_1 - a_2 c_2) + y^2 \ln \left| \frac{a_1 + c_1}{a_2 + c_2} \right| \right] dy$$

$$a_1 = \rho_{opt} + L/2$$

392 $\quad a_2 = \rho_{opt} - L/2 \qquad\qquad\qquad\qquad\qquad\qquad\qquad\qquad\qquad\qquad\qquad$ (A.6)

$$c_1 = \sqrt{a_1^2 + y^2}$$

$$c_2 = \sqrt{a_2^2 + y^2}$$

393   Eq. (A.6) can be integrated between the limits $-W/2$ to $W/2$ using classical numerical integration

394   formulas.

1 REFERENCES

2 Bransby, M. F., and Randolph, M. F. (1998). "Combined loading of skirted foundations."

3 *Géotechnique*, 48(5), 637-655.

4 Chen, W. F., and Liu, X. L. (1990). *Limit analysis and soil plasticity*. Elsevier Publishing

5 Co., Amsterdam, The Netherlands.

6 Feng, X., Randolph, M. F., Gourvenec, S. and Wallerand, R. (2014). "Design approach for

7 rectangular mudmats under fully three-dimensional loading", *Geotechnique*, 64(1), 51-63.

8 HKS Inc. (2008). *ABAQUS Version 6.6 User's Manual*. Hibbitt, Karlson and Sorensen, Inc,

9 Pawtucket, Rhode Island.

10 Murff, J. D., Randolph, M. F., Elkhatib, S., Kolk, H. J., Ruinen, R. M., Strom, P. J., and

11 Thorne, C. P. (2005). "Vertically loaded plate anchors for deepwater applications." *Proc.*

12 *Int. Symp. on Frontiers in Offshore Geotechnics: ISFOG 2005,* Perth, Australia, 31-48.

13 Nouri, H., Biscontin, G., Aubeny, C. (2014). "Undrained bearing capacity of shallow founda-

14 tions under combined sliding and torsion," A*SCE Journal of Geotechnical and*

15 *Geoenvironmetal Engineering*. Vol. 140, No. 8.

16 Nouri., H. (2013). *Numerical Methods in Offshore Geotechnics: Applications to Submarine*

17 *Landslides and Anchor Plates*. Doctoral dissertation, Texas A&M University.

18 O'Neill, M. P., Bransby, M. F., and Randolph, M. F. (2003). "Drag anchor fluke-soil interac-

19 tion in clays." *Can. Geotech. J.*, 40, 78-94.

20 Rowe, R. K. and Davis, E. H. (1977). *Application of the finite element method to the predic-*

21 *tion of collapse loads.* Research Report R310. Sydney: University of Sydney.

22 Song, Z., Hu, Y., and Randolph, M. F. (2008). "Numerical simulation of vertical pullout of

23 plate anchors in clay." *J. Geotech. Geoenviron.*, 134(6), 866-875.

24 Van Langen, H., Vermeer, P.A. (1991). "Interface elements for singular plasticity points." *Int.*

25 *J. Numer. Anal. Met.*, 15(5), 301-315.

1 Wang, D., Hu, Y., and Randolph, M. F. (2010) "Three-dimensional large deformation finite

2   element analysis of plate anchors in uniform clay." *J. Geotech. Geoenviron.*, 136(2), 355-

3   365.

4 Wei, Q., Tian, Y., Cassidy, M. J., Gaudin, C. and O'Loughlin, C. D. (2015). "Behaviour of

5   OMNI-Max anchors under chain loading." *The 3rd International Symposium on Frontiers*

6   *in Offshore Geotechnics*. Oslo, Norway.

7 Yang, M., J. Murff, and Aubeny, C. P., (2010). "Undrained Capacity of Plate Anchors under

8   General Loading." *J. Geotech. Geoenviron.*, 136(10), 1383-1393.

List of Figures:

Fig. 1- Applied loads to idealized plate anchor: (a) pull-out force in normal operating condition; (b) general six degrees of freedom loading after extreme loading condition

Fig. 2- Normalized shear load-displacement for different 2D-FE meshes

Fig. 3- Section view of the x-displacement contours for a plate under pure sliding

Fig. 4- Contours of displacement magnitudes for a plate under pure torsion: (a) plan view (b) isometric section A-A

Fig. 5- Final 2D finite element mesh for a strip plate of $t = L/20$

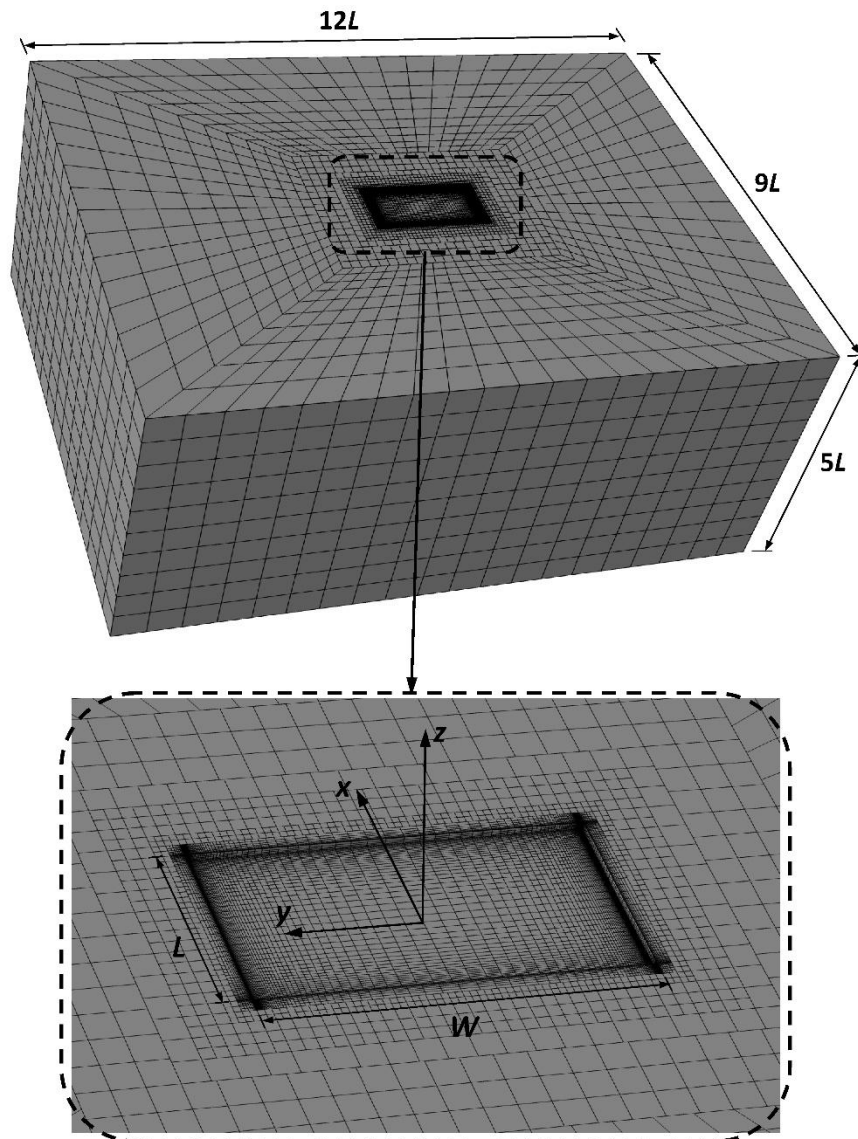Fig. 6- Ultimate shear capacity versus log of friction coefficient

Fig. 7- A typical 3D finite element mesh for a rectangular plate

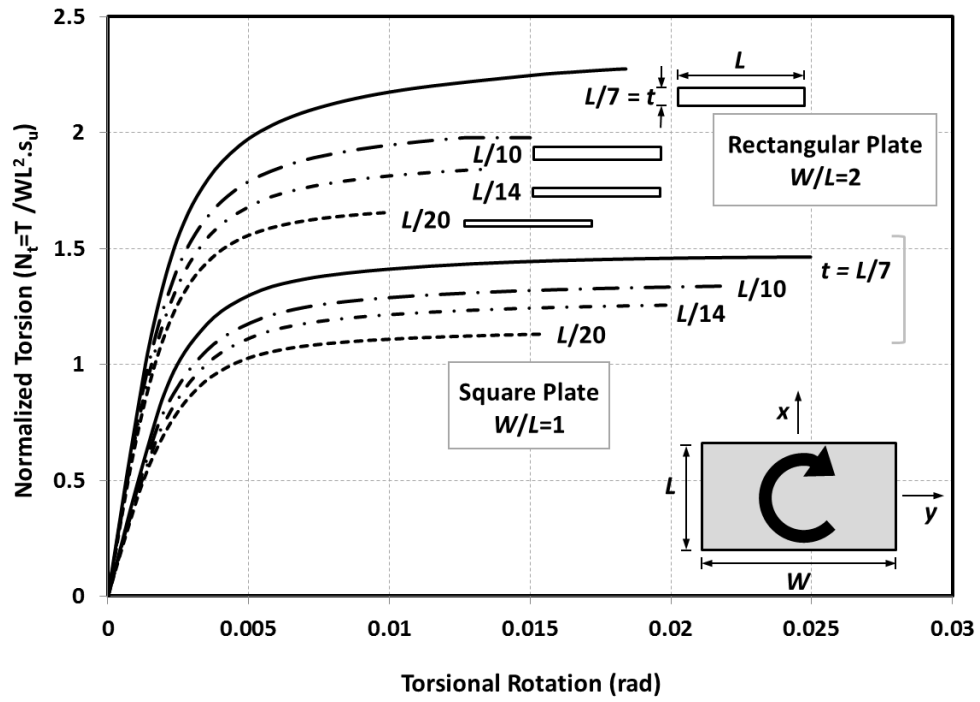Fig. 8- Load-displacement curves for plates under y-translation: (a) square; (b) rectangular (W/L=2) plates

Fig. 9- Torsion-rotation plots for square and rectangular plates

Fig. 10- Typical FE shear$y$-torsion failure envelopes for: (a) square; (b) rectangular plates

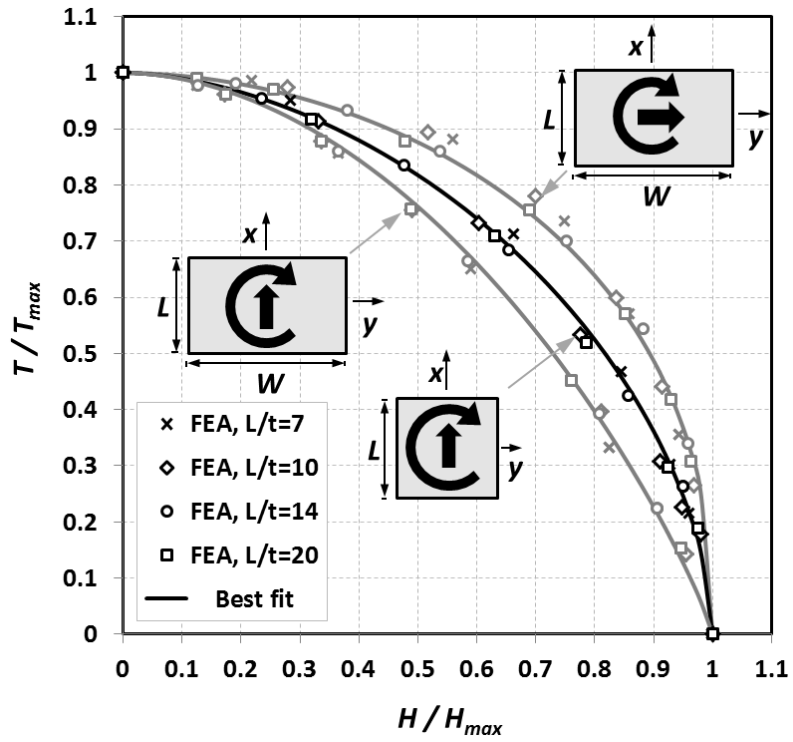Fig. 11- FE normalized failure envelopes for plates under combined shear-torsion

Fig. 12- FE vs PLA$_{t=0}$ normalized failure envelopes for plates under combined shear-torsion

Fig. 13- FE shear resistance reduction with eccentricity: (a) example of ultimate resistance for plates of t=L/7; (b) normalized resistance for plates of various thicknesses

Fig. 14- Typical FE failure envelopes for plate subjected to co-planar shear (shearx-sheary)

Fig. 15- FE normalized failure envelopes for plates under co-planar shear

Figure A.1- Model for PLA virtual work approach for zero thickness plate (PLA$_{t=0}$) under combined sliding-torsion
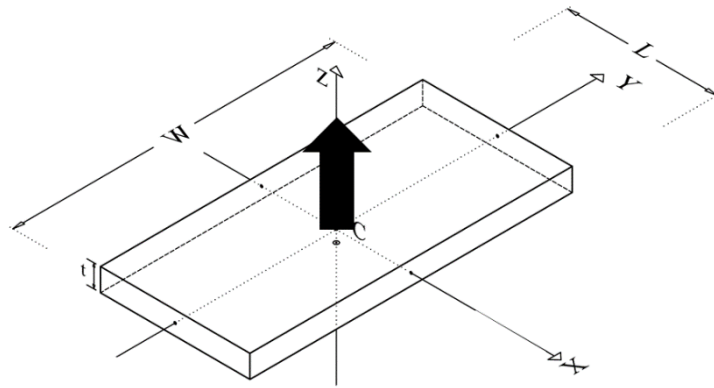
(a)
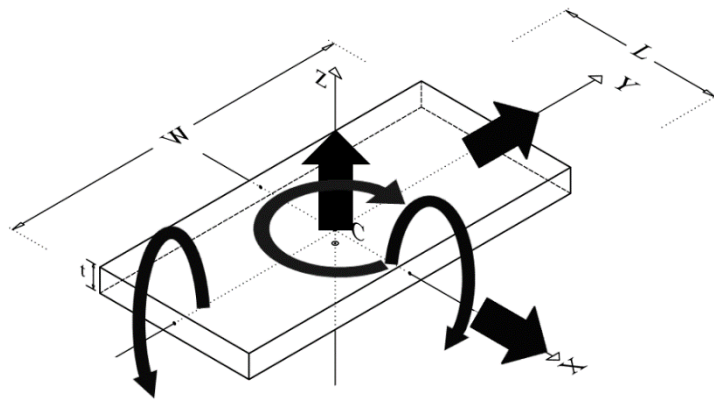
(b)

Fig. 1- Applied loads to idealized plate anchor: (a) pull-out force in normal operating condition; (b) general six degrees of freedom loading after extreme loading condition
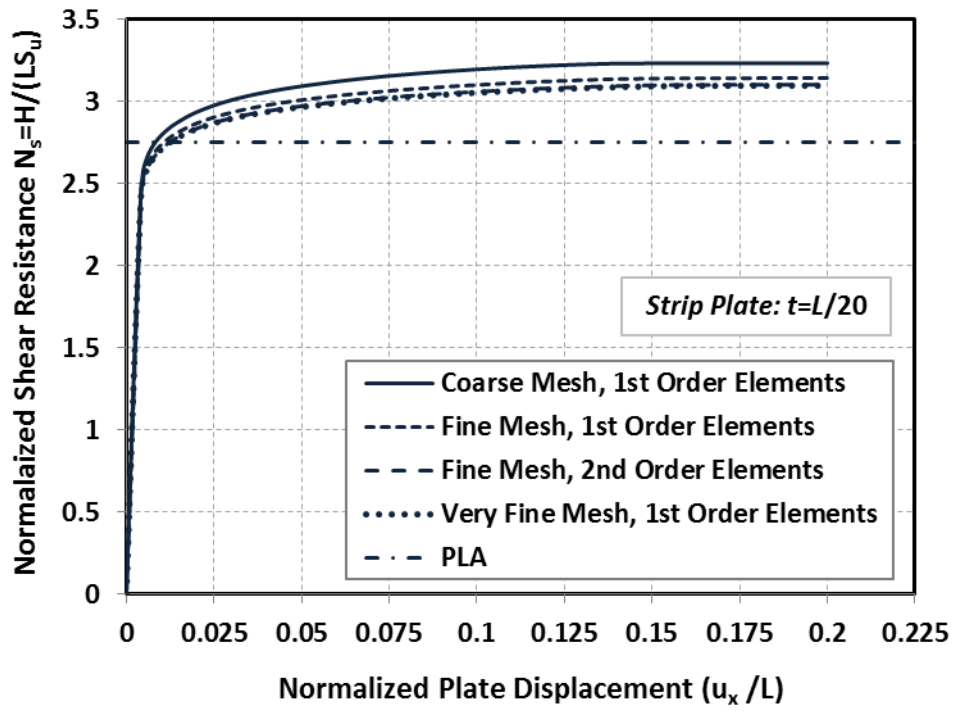
Fig. 2- Normalized shear load-displacement for different 2D-FE meshes
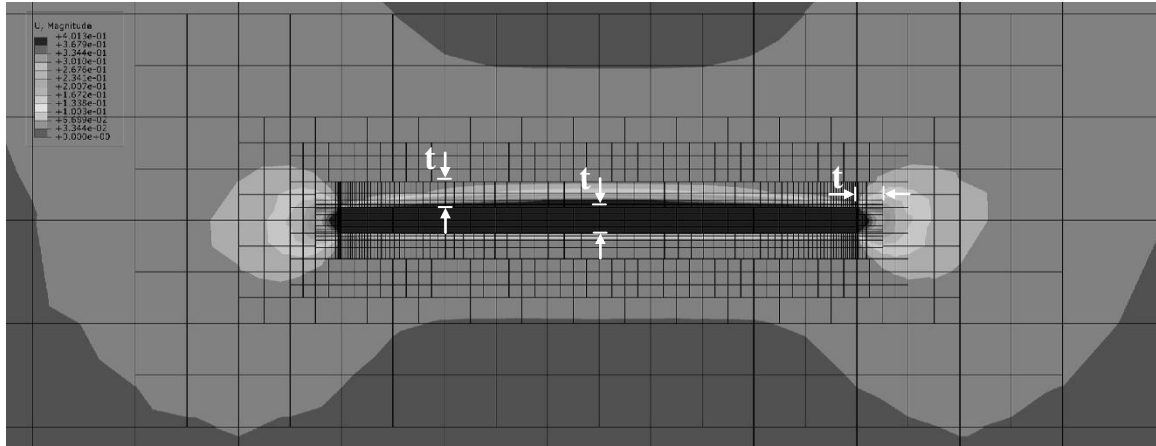
Fig. 3- Section view of the *x*-displacement contours for a plate under pure sliding
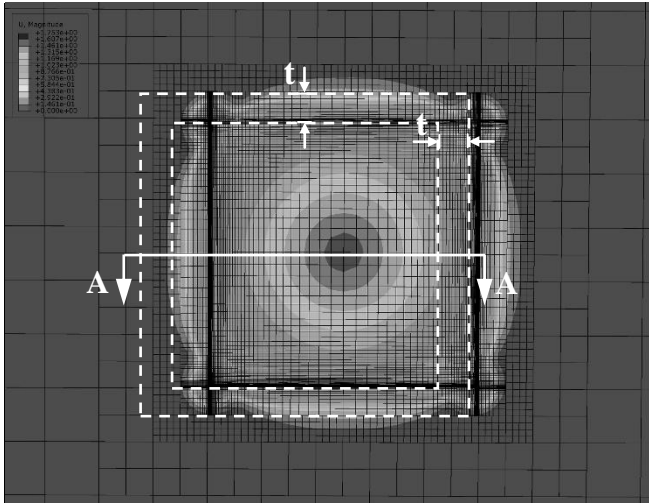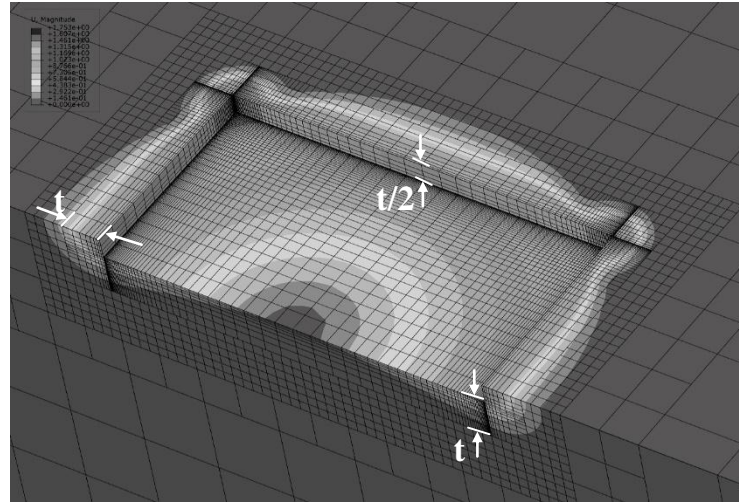
(a)　　　　　　　　　　　　　　　　　　　(b)

Fig. 4- Contours of displacement magnitudes for a plate under pure torsion:

(a) plan view (b) isometric section A-A
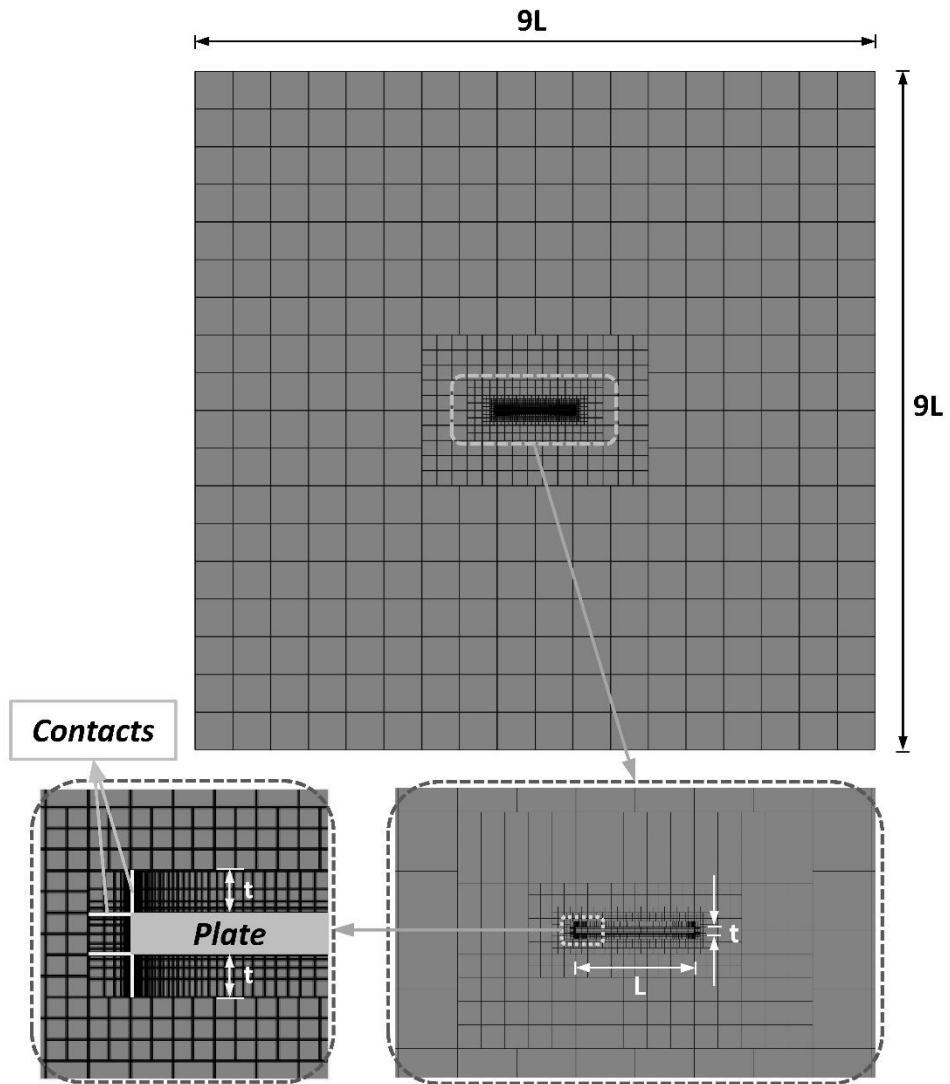
Fig. 5- Final 2D finite element mesh for a strip plate of *t =L*/20
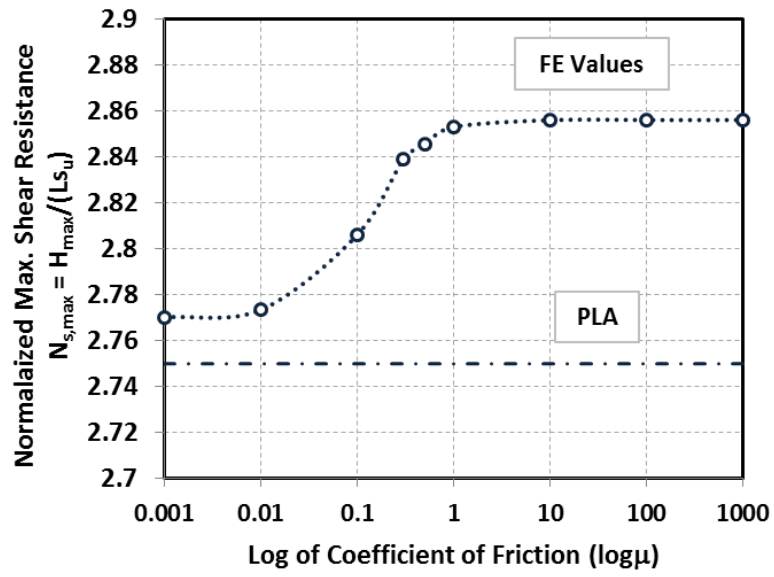
Fig. 6- Ultimate shear capacity versus log of friction coefficient

Fig. 7- A typical 3D finite element mesh for a rectangular plate
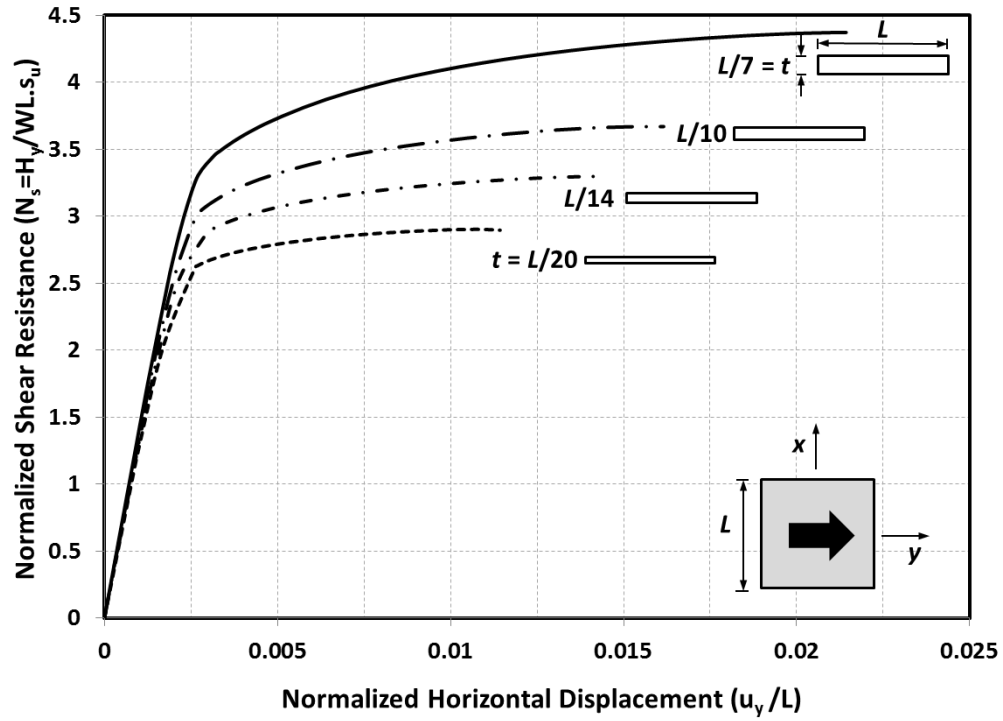
(a)
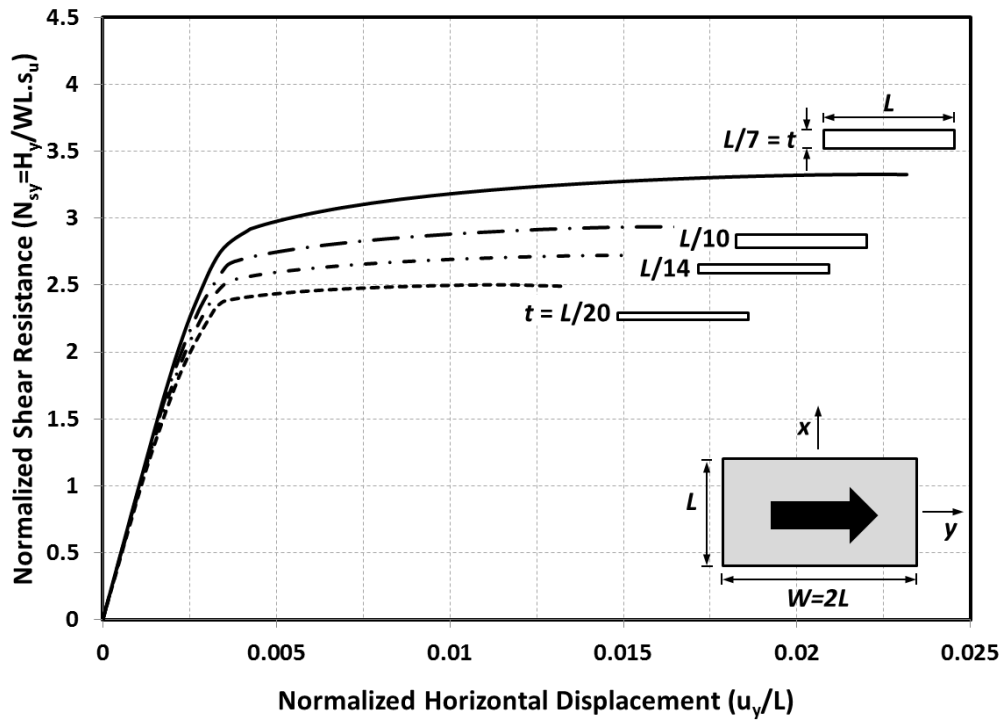
(b)

Fig. 8- Load-displacement curves for plates under *y*-translation: (a) square; (b) rectangular (*W*/*L*=2) plates

Fig. 9- Torsion-rotation plots for square and rectangular plates
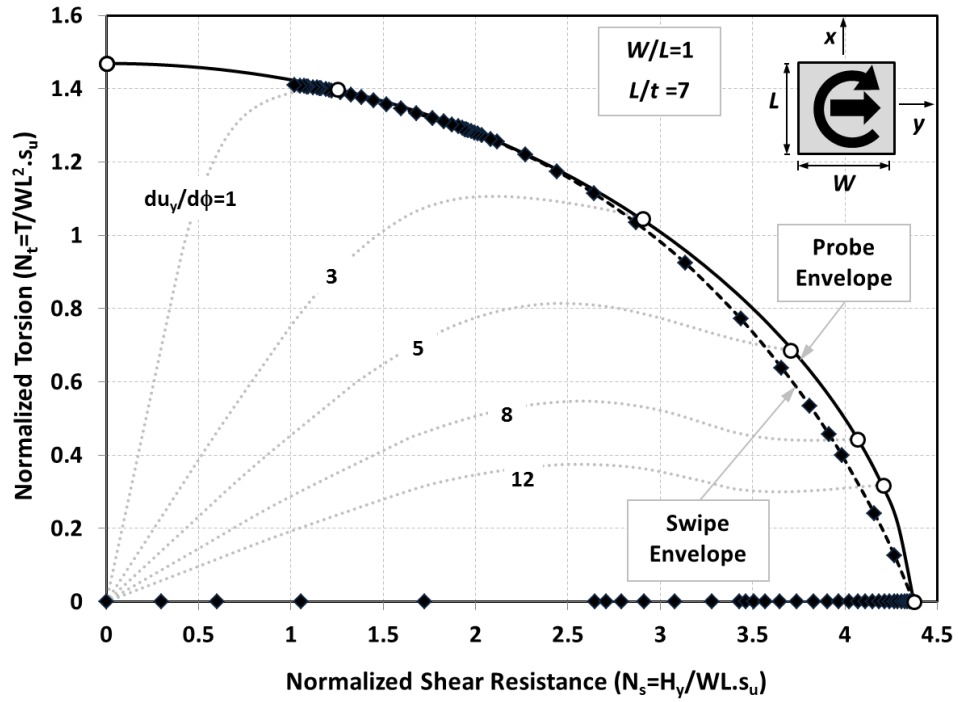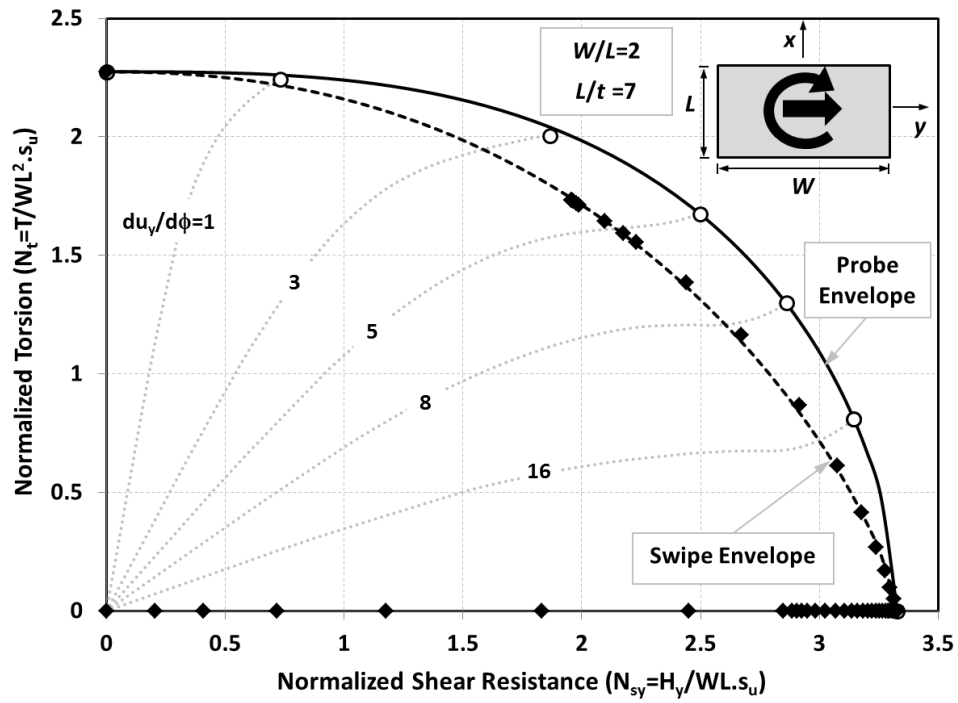
Fig. 10- Typical FE sheary-torsion failure envelopes for: (a) square; (b) rectangular plates

Fig. 11- FE normalized failure envelopes for plates under combined shear-torsion
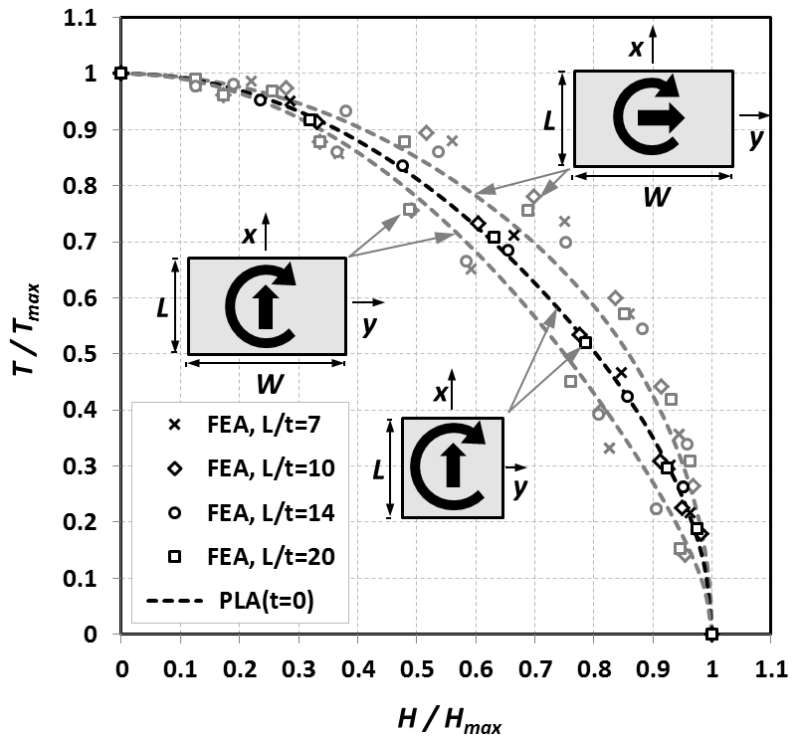
Fig. 12- FE vs PLA$_{t=0}$ normalized failure envelopes for plates under combined shear-torsion

(a)

(b)

Fig. 13- FE shear resistance reduction with eccentricity: (a) example of ultimate resistance for plates of t=L/7; (b) normalized resistance for plates of various thicknesses
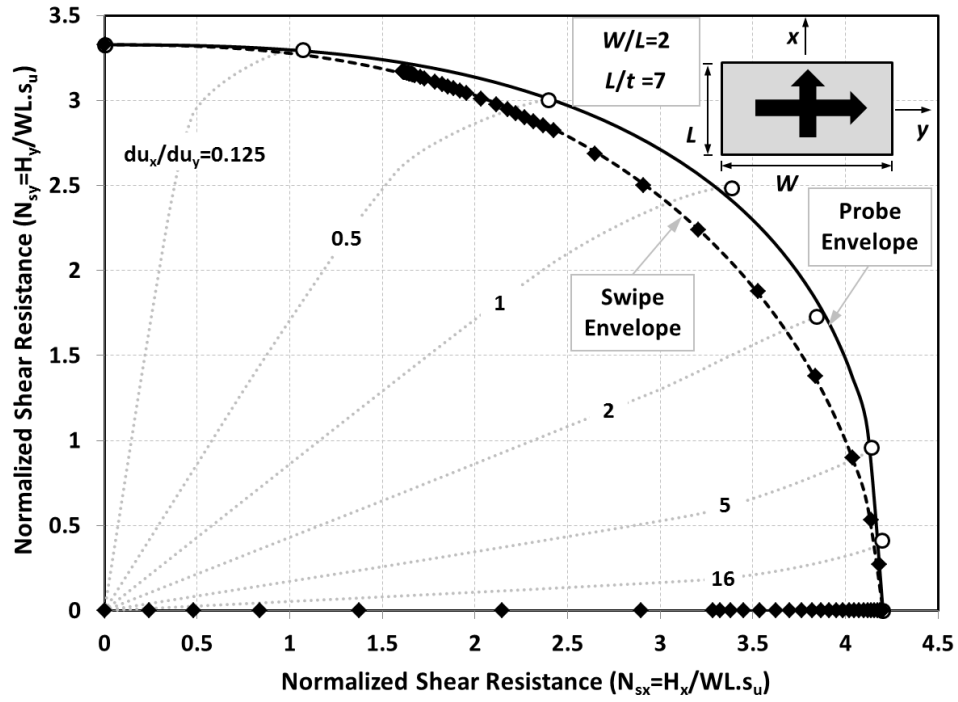
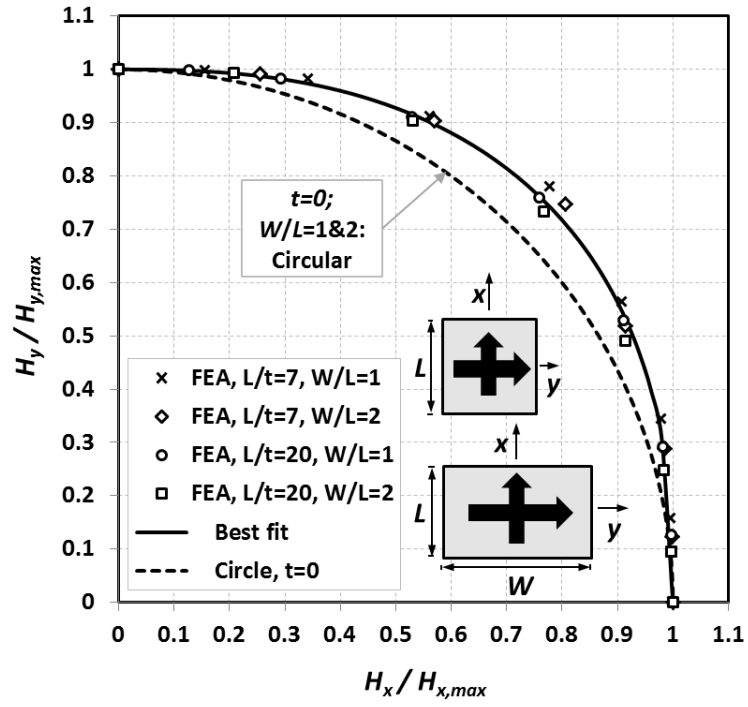Fig. 14- Typical FE failure envelopes for plate subjected to co-planar shear (shearx-sheary)

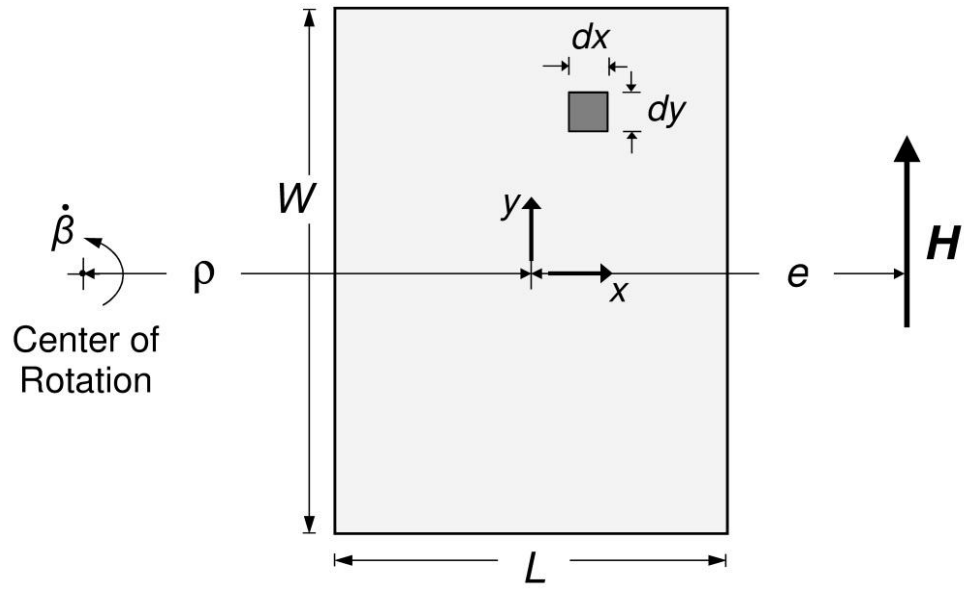Fig. 15- FE normalized failure envelopes for plates under co-planar shear

Figure A.1- Model for PLA virtual work approach for zero thickness plate (PLA$_{t=0}$) under combined sliding-torsion